J. Fluid Mech. (2019), *vol.* 880, *pp.* 32–58.
doi:10.1017/jfm.2019.687

Contrasts between momentum and scalar transport over very rough surfaces

Qi Li[1,2,†] **and Elie Bou-Zeid**[2]

[1]Department of Civil and Environmental Engineering, Princeton University, Princeton, NJ 08544, USA

[2]School of Civil and Environmental Engineering, Cornell University, Ithaca, NY 14853, USA

(Received 6 December 2018; revised 10 August 2019; accepted 10 August 2019;
first published online 7 October 2019)

Large-eddy simulations are conducted to contrast momentum and passive scalar transport over large, three-dimensional roughness elements in a turbulent channel flow. Special attention is given to the dispersive fluxes, which are shown to be a significant fraction of the total flux within the roughness sublayer. Based on pointwise quadrant analysis, the turbulent components of the transport of momentum and scalars are found to be similar in general, albeit with increasing dissimilarity for roughnesses with low frontal blockage. However, strong dissimilarity is noted between the dispersive momentum and scalar fluxes, especially below the top of the roughness elements. In general, turbulence is found to transport momentum more efficiently than scalars, while the reverse applies to the dispersive contributions. The effects of varying surface geometries, measured by the frontal density, are pronounced on turbulent fluxes and even more so on dispersive fluxes. Increasing frontal density induces a general transition in the flow from a wall bounded type to a mixing layer type. This transition results in an increase in the efficiency of turbulent momentum transport, but the reverse occurs for scalars due to reduced contributions from large-scale motions in the roughness sublayer. This study highlights the need for distinct parameterizations of the turbulent and dispersive fluxes, as well as the importance of considering the contrasts between momentum and scalar transport for flows over very rough surfaces.

Key words: turbulent boundary layers

1. Introduction

The dynamics of turbulent shear flows over rough walls has been an active area of research because of its relevance in the design of engineering systems and in environmental fluid mechanics. Momentum and scalar exchanges between the wall and the fluid in such flows are of interest in a wide range of disciplines (Belcher, Harman & Finnigan 2012). Previous field experiments over natural vegetation (Katul *et al.* 1997*b*; Poggi, Katul & Albertson 2004), wind tunnel studies over obstacles of regular shapes (Macdonald & Griffiths 1998; Castro, Cheng & Reynolds 2006) and numerical simulations over three-dimensional roughness elements (Coceal *et al.*

† Email address for correspondence: ql56@cornell.edu

2007*a*; Finnigan, Shaw & Patton 2009; Leonardi *et al.* 2015) have advanced our understanding of this problem significantly. For example, these past studies have underlined the importance of dispersive fluxes inside and close to the roughness elements (Poggi *et al.* 2004; Poggi & Katul 2008; Jelly & Busse 2018). Nevertheless, there still remains a significant knowledge gap, particularly concerning the transport of scalars, and how it compares to that of momentum, over surfaces that consist of 'large' three-dimensional bluff-body-type roughness elements. Large here implies that the roughness protrudes significantly into the inertial sublayer, and that the details of the flow below the top of the roughness elements are important for the application. Note that in the atmospheric science literature, the inertial sublayer is often called the 'surface layer'. Over a rough wall, it would be found above the canopy sublayer (ranging from the ground to the top of the roughness elements) and the roughness sublayer (ranging from the top of the roughness elements up to the height where the flow signatures of individual roughness elements are blended out). In the review paper by Jiménez (2004), he limited the discussions of rough-wall boundary layers to $H/\delta < 0.025$, where H is the roughness element height and δ is depth of the boundary layer. In many natural settings and engineering applications, H/δ often exceeds 0.1, a regime sometimes termed the very rough surface (Castro *et al.* 2006). For very rough surfaces, momentum and scalar transport within the canopy and roughness sublayers are topics of active ongoing research.

Various previous numerical studies (e.g. Kanda, Moriwaki & Kasamatsu 2004; Castro *et al.* 2006; Coceal *et al.* 2007*a*; Orlandi & Leonardi 2008; Anderson, Li & Bou-Zeid 2015; Anderson 2016; Giometto *et al.* 2016; Li, Bou-Zeid & Anderson 2016*a*; Li *et al.* 2016*b*) have probed the details of these very rough-wall flows such as the morphology of coherent structures and the effects of the roughness in such regimes. Moreover, recent large-eddy simulations (LES) and direct numerical simulations (DNS) (Finnigan *et al.* 2009; Boppana, Xie & Castro 2010, 2012; Park & Baik 2013; Philips, Rossi & Iaccarino 2013; Leonardi *et al.* 2015; Li *et al.* 2016*b*) investigated the transport of scalars. However, compared to the extensive literature focusing on the flow and momentum transport, research on scalars and their transport in flows over very rough walls remains quite limited. In addition, a detailed comparative analysis of momentum and scalar transport dynamics has not been performed before.

These open gaps motivate this present paper: we investigate both momentum and scalars at very high Reynolds numbers over three-dimensional, large roughness using the LES technique. We focus on the canopy and roughness sublayers. A logarithmic layer will exist further aloft if the roughness sublayer does not extend all the way to the top of the inertial layer. In particular, the analyses concern two aspects of the problem: the effects of different roughness geometries and the comparison between momentum and scalar transport. The numerical set-up of the problem is described next in § 2. Section 3 reports the results on the changes in turbulent flow characteristics for different surface geometries (§ 3.1) and on the spatially coherent dispersive fluxes, in particular, the differences between momentum and scalar transport (§ 3.2). Section 4 concludes with a summary and discussion.

2. Numerical set-up

In the LES code, the non-dimensional filtered incompressible continuity (2.1), Navier–Stokes (2.2), and scalar conservation (2.3) equations are solved assuming hydrostatic equilibrium of the mean flow,

$$\frac{\partial u_i}{\partial x_i} = 0, \tag{2.1}$$

$$\frac{\partial u_i}{\partial t} + u_j\left(\frac{\partial u_i}{\partial u_j} - \frac{\partial u_j}{\partial u_i}\right) = -\frac{\partial p}{\partial x_i} - \frac{\partial \tau_{ij}}{\partial x_j} + F_i + B_i, \tag{2.2}$$

$$\frac{\partial \theta}{\partial t} + u_i\frac{\partial \theta}{\partial x_i} = -\frac{\partial q_i^s}{\partial x_i}. \tag{2.3}$$

All the variables we will discuss are filtered components, so the usual tilde above the symbols is omitted for simplicity. The density ρ is taken to be unity and is uniform: buoyancy forces are not considered. x, y and z denote the streamwise, cross-stream and wall-normal directions respectively, and u, v and w are the velocity components in these respective directions. t denotes time; u_i is the resolved velocity vector; x_i is the position vector; p is a modified pressure that includes the resolved and subgrid scale (SGS) kinetic energy (Bou-Zeid, Meneveau & Parlange 2005); τ_{ij} is the deviatoric part of the SGS stress tensor; F_i is the body force driving the flow (here simply a homogeneous steady horizontal pressure gradient along the x direction with magnitude $u_*^2/\rho\delta$). The code uses the immersed boundary method (IBM) to account for the presence of the roughness elements via an immersed boundary force B_i. Here we adopt a discrete forcing approach to compute B_i (Mohd-Yusof 1997), which means that the effect of the immersed boundary is incorporated into the discretized governing equations and B_i is estimated *a priori*, improving numerical stability (Mittal & Iaccarino 2005; Mittal *et al.* 2008; Fang *et al.* 2011). The specific implementation in the code used here is detailed and validated in Tseng, Meneveau & Parlange (2006), Chester, Meneveau & Parlange (2007) and Li *et al.* (2016*a*,*b*). A friction velocity of $u_* = 1$ ms^{-1}, and a half-channel width of $\delta = 100$ m, are the nominal values used to non-dimensionalize t and all outputs of the code; their imposed numerical values are thus inconsequential here. The top boundary is impermeable with zero stress; the simulations therefore are similar to a half-channel. In (2.3), θ denotes a passive scalar quantity, which for illustration is considered to be temperature in Kelvin in the current simulations, and q_i^s is the ith component of the SGS scalar flux.

We used the Lagrangian scale-dependent dynamic subgrid-scale model (Bou-Zeid *et al.* 2005, 2008) to compute the SGS viscosity required for modelling τ_{ij}. Using a constant subgrid-scale Prandtl number of 0.4 (Kang & Meneveau 2001; Bou-Zeid *et al.* 2010; Li 2016), the SGS diffusivity needed for q_i^s is then calculated. Detailed validations for the flow and scalar transport can be found in Li *et al.* (2016*a*) and Li *et al.* (2016*b*), respectively. The LES uses a wall model for momentum and scalars that has been developed for a hydrodynamically smooth wall (here each facet of a building/cube is such a smooth wall) at high Reynolds numbers based on Kader & Yaglom (1972). For the wall model, Reynolds analogy in the vicinity of the wall (the unresolved viscous and buffer layers) is invoked. Wall modelling for complex topographies remains an ongoing area of research (Yang *et al.* 2015) and an open challenge (Bose & Park 2018). However, the performance of the current approach has been evaluated and shown to be quite satisfactory in Li *et al.* (2016*b*). Note also that although the viscous and diffusive terms are omitted in (2.2) and (2.3), the Reynolds number is encapsulated in the wall model. The friction Reynolds number $Re_* = (u_*\delta)/\nu$ is approximately 10^7 for all LES runs, where ν is the kinematic viscosity of air used in the wall model. Since the paper does not focus on the effect of different thermal boundary conditions, which has been studied in Pirozzoli, Bernardini & Orlandi (2016), a constant surface temperature scalar boundary condition is used for the surfaces of the obstacles and the bottom wall; the top thermal boundary condition is zero flux.

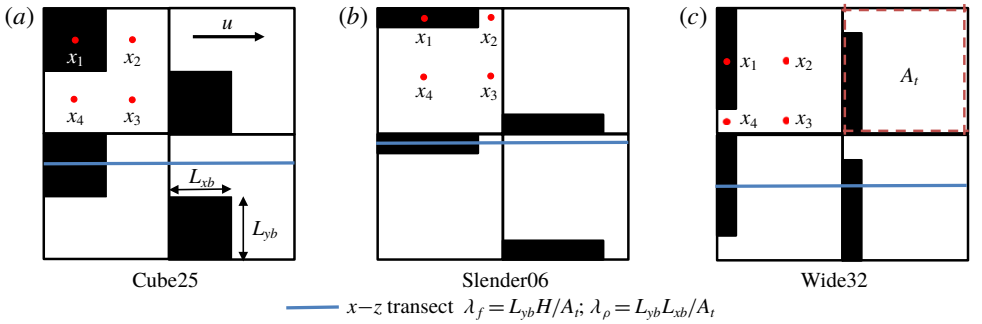

FIGURE 1. (Colour online) Top view of the 'repeating unit' for three cases shown in table 1, where shaded areas represent the obstacles: (*a*) Cube25; (*b*) Slender06; (*c*) Wide32. Area highlighted by red-dotted line is the lot area, A_t. Different intermediate cases labelled as Sf in table 1 are achieved through varying L_{xb} and L_{yb} while keeping H, the obstacle height, constant. Frontal area density, λ_f, and plan area density λ_p are defined. Points labelled as x_1 to x_4 (red dots) represent locations where time series of instantaneous data are recorded for analysis. For consistency, we refer to the locations for points x_1 to x_4 as 'on top', 'behind', 'in front' and 'in between' the obstacle, respectively, for all cases.

Case	λ_p	λ_f	N_x^b, N_y^b, N_z^b	N_x, N_y, N_z	L_x/δ	L_y/δ
Cube25	0.25	0.25	8, 8, 8	192, 96, 64	3	1.5
Slender06	0.12	0.06	16, 3, 8	200, 100, 64	3.125	1.5625
Sf08	0.12	0.08	12, 4, 8	200, 100, 64	3.125	1.5625
Sf12	0.12	0.12	8, 6, 8	200, 100, 64	3.125	1.5625
Sf16	0.12	0.16	6, 8, 8	200, 100, 64	3.125	1.5625
Sf24	0.12	0.24	4, 12, 8	200, 100, 64	3.125	1.5625
Wide32	0.12	0.32	3, 16, 8	200, 100, 64	3.125	1.5625

TABLE 1. Summary of simulation parameters. $H/\delta = 0.125$ across all cases, where H is the height of obstacles. δ, the half-channel, is set equal to the domain height L_z. N_i^b is the number of grid points resolving one obstacle in the i direction, while N_i is the total number of computational points in that direction. L_x and L_y are the domain dimensions in the streamwise and cross-stream directions. The two digits at the end of each case name are $\lambda_f \times 100$ for that case. Sf stands for 'Stagger frontal'.

To explore the effects of the geometry, we conducted simulations of different cases as summarized in table 1 and illustrated in figure 1. The parameters λ_f and λ_p are the frontal area ratio and plan area ratio, respectively; λ_f is defined as the total projected frontal (mean-flow normal) area of the roughness elements per unit wall-parallel area (i.e. land area) and λ_p is the ratio between the crest plan area (i.e. roof area, shaded in black figure 1) and the wall-parallel area. The first case is the classic cubical obstacles. In the remaining cases, we gradually change the horizontal aspect ratio of the obstacles, while maintaining the same height and area (λ_p). Figure 1 shows the cubical case and the two extreme aspect ratios of the other cases. All cases shown in table 1 were run for 50 eddy turnover times ($T \approx \delta/u_*$) and averaged for the last 25 T. The averaging time is comparable to that in Leonardi & Castro (2010), where averaging was done over $2000T_b$ for $T_b = H/U_b$; U_b is the bulk streamwise velocity and H is the obstacle height. Throughout the paper and unless otherwise noted, $\langle X \rangle$

defines a volume average of X over $L_x L_y \Delta z$, where Δz is the vertical grid size; $\overline{X}$ defines a temporal average of X. A single prime ($'$) denotes deviation from $\overline{X}$, where $X = \overline{X} + X'$. A double prime ($''$) denotes deviation from $\langle \overline{X} \rangle$, where $\overline{X} = \langle \overline{X} \rangle + \overline{X}''$.

A sensitivity test was carried out to examine the effect of the number of points used to represent the obstacles and the domain length, particularly for cases where one dimension of the cubes is only spanned by three grid points. The comparisons for case Wide32 between the original simulation, a doubled resolution run and a run with doubled L_x are shown in appendix A. The two simulations with different resolutions show converging results for the turbulent fluxes in the canopy and roughness sublayers. Although some discrepancies exist for the dispersive contributions, the conclusions reached in the present study regarding the Reynolds stress, turbulent scalar flux, dispersive fluxes and the quadrant analysis are insensitive to doubling the grid resolution and the streamwise dimension the computational domain.

3. Results and discussion

3.1. *Turbulent transport*

3.1.1. *Effects of surface geometry*

We first focus on the impact of surface geometry on the general turbulent flow characteristics. The parameter space that characterizes the surface geometry is large. A non-exhaustive list of previous studies have investigated height variations (Yang *et al.* 2016), geometric shapes (Leonardi *et al.* 2015; Yang *et al.* 2016; Llaguno-Munitxa, Bou-Zeid & Hultmark 2017; Llaguno-Munitxa & Bou-Zeid 2018) of regular (Kanda *et al.* 2004; Placidi & Ganapathisubramani 2015) or irregular (Chester *et al.* 2007; Yuan & Jouybari 2018) surface roughness elements, as well as statistical moments of roughness elements (Zhu *et al.* 2017). We do not aim to comprehensively examine the parameter space in this paper, but we are more interested in the general transition of the flow as the roughness, conserving the same area density λ_p, changes from slender elements with low λ_f to wide ones with high λ_f. Ghisalberti (2009) analysed the dynamics of flows over many different types of canopies and used the term 'obstructed shear flows' to describe them; he concluded that this type of canopy flow can be characterized by the penetration depth (δ_e) of the vortices into the canopy sublayer. Inflection points in $\langle u \rangle / u_*$ clearly exist across all cases, especially with increasing λ_f as shown in figure 2(*a*). Figure 2(*b*) shows the shear scale L_s, which can serve as an estimate of δ_e, as a function of the frontal blockage ratio λ_f. L_s is a basic length scale in canopy flows similar to the vorticity thickness defined in a plane mixing layer; it is defined as $L_s = \langle \bar{u} \rangle / \langle \mathrm{d}\bar{u}/\mathrm{d}z \rangle$, here computed at $z = H$. The value of L_s, and consequently δ_e, decreases with increasing λ_f (figure 2*b*), which signifies a larger shear strength and hence larger deviation from the classical rough-wall boundary-layer flow as the blockage increases. L_s for Slender06 and Wide32 differ significantly and additional intermediate cases show a monotonic decrease with λ_f, which are consistent with the mean streamwise velocity profiles in figure 2(*a*).

The correlation coefficient r_{uw}, computed as $\langle (\overline{u'w'})/(\sigma_u \sigma_w) \rangle$ at $z = H$, is also depicted in figure 2(*b*). Its magnitude can be interpreted as a vertical turbulent momentum transport efficiency (Li & Bou-Zeid 2011). As λ_f increases, $-r_{uw}$ increases approximately from 0.2 to 0.46, the latter being consistent with what is typically found in canopy flows and mixing layers ($-r_{uw} \approx 0.5$) (Finnigan 2003). At a higher elevation of $z/H = 1.5$, r_{uw} for case Slender06 recovers to 0.43 (not shown here), consistent with observations over a smoother water surface (with negligible influence of surface waves) in the atmospheric inertial sublayer under neutral stratification

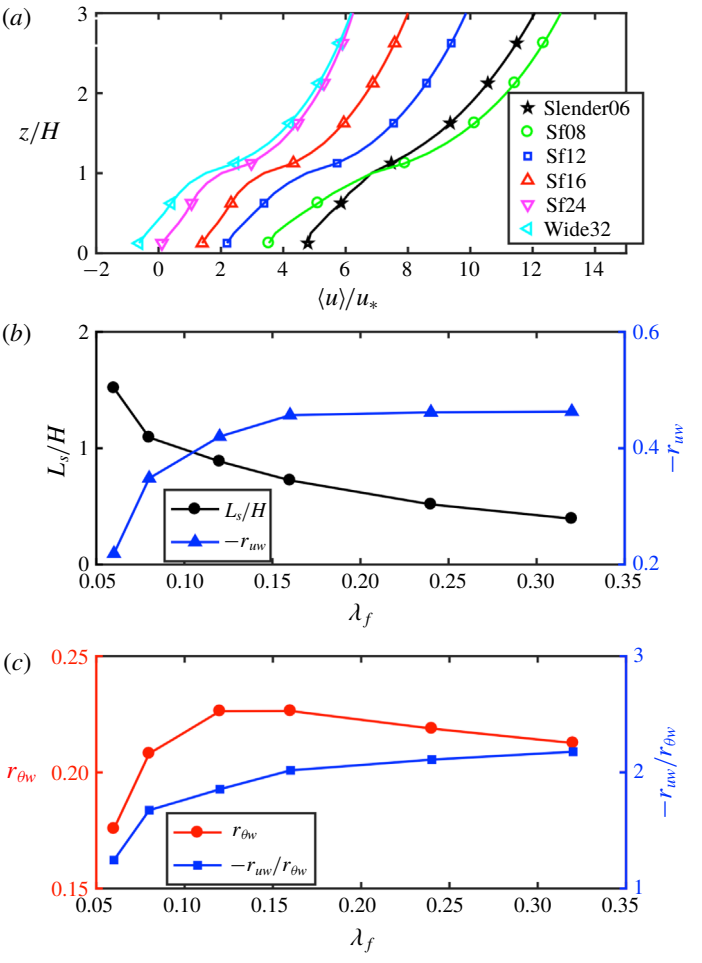

FIGURE 2. (Colour online) (*a*) Value of $\langle u\rangle/u_*$ as a function of z/H, where inflection points are present at $z/H > 1$; (*b*) shear length scale L_s and the correlation coefficient r_{uw} for cases listed in table 1 (except cube25) computed at $z = H$; (*c*) $r_{\theta w}$ and $r_{uw}/r_{\theta w}$ for the same cases as (*a*).

(Li & Bou-Zeid 2011). It is worth reiterating that obstacles in all the cases presented in figure 2 have the same plan area density (i.e. $\lambda_p = 0.12$); but by changing λ_f, we are observing a transition from a canonical wall-bounded flow to a free shear flow, akin to a mixing layer, where momentum turbulent transport is more efficient.

As this transition occurs, and unlike for its momentum counterpart, the vertical transport efficiency for the scalar exhibits a non-monotonic behaviour (figure 2*c*), reaching a peak of approximately 0.23 at around $\lambda_f = 0.12$. For large λ_f, while momentum r_{uw} is more than twice larger than its value at $\lambda_f = 0.06$, the scalar $r_{\theta w}$ changes less significantly with changing geometry. Overall, the results show that, as the flow becomes more mixing layer like, the momentum and scalar transport efficiencies increasingly diverge. The ratio of their correlation coefficients becomes appreciably larger than 1 (figure 2*c*), making the Reynolds analogy (which postulates that momentum and scalars are transported similarly) less applicable. Note that we

do not imply that the flow over a very rough wall or vegetation canopy completely resembles the canonical mixing-layer flow. Rather, the examples shown in the present study demonstrate that the rough wall-bounded flows can exhibit mixed properties of wall-bounded and mixing layer flows (Kanda 2006).

To gain a better understanding of the turbulent statistics at representative points with respect to the roughness elements, we sampled data at four different points x_1–x_4 (see figure 1) for all heights. The pointwise time series of relevant quantities are recorded at a frequency of $1/(2500T)$, where T is the eddy turnover time defined previously. Data were sampled at each time step for a total period of $2T$. This time averaging alone is not sufficiently long to guarantee complete statistical convergence of the results. However, the statistics were also phase averaged for all repeating units to improve statistical convergence and the primary characteristics of the flow that we will focus on are already very clear with this averaging scheme. Turbulent fluctuations tend to be non-Gaussian for canopy flows over vegetation surfaces (Raupach 1981; Rotach 1993; Finnigan 2003; Chamecki 2013). The skewness of a fluctuating component is an indication of the dominance of either positive or negative events given its probability distribution. As pointed out in Mouri *et al.* (2003) in a laboratory experiment of rough-wall-bounded flow over cubical arrays, the wakes associated with the roughness elements result in correlations between the Fourier modes of the energy-containing eddies, whereas the Fourier modes are independent and random for the case of Gaussian turbulence. To further investigate the transition from a wall-bounded to a mixing-layer flow regime, first, we computed the skewness of the fluctuating components shown in figure 3(*a–c*) for point x_3 for u/u_*, w/u_* and θ/θ_1, where $\theta_1 = \theta(z = \delta)$. We only illustrate three cases with the same λ_p, spanning the full range of λ_f. Slender06 has close to zero skewness for u' and w' (figure 3*a*,*b*) in the roughness sublayer but higher values are observed as λ_f increases in cases Sf16 and Wide32, more typical of canopy flows from experimental measurements over vegetation canopies (Raupach 1981; Rotach 1993; Finnigan 2003). The variation in skewness from small values in Slender06 to larger ones as λ_f increases is consistent with what is expected based on the characteristics of wall-bounded and mixing-layer flows shown in table 2 of Finnigan (2003). In figure 3(*d–f*), the kurtosis Ku_u and Ku_θ tends to approach 3 away from the roughness, deviating from that Gaussian value as the wall is approached. An exception is the u' kurtosis of cases Sf16 and Wide32, which is closer to 3 in the canopy sublayer. However, it should be noted that a kurtosis of 3 is a necessary but not a sufficient condition for the fluctuations to be Gaussian (a bimodal distribution could also have a kurtosis of 3). Two final observations on figure 3: (i) the skewness and kurtosis of θ are much less sensitive to geometry, in agreement with the findings based on the transport efficiency in figure 2, and (ii) while the skewness plots suggest a convergence of the various geometries at $z/H \approx 2$, the kurtosis continues to show significant differences at that height.

Since in physical space we observed that changes in surface roughness modify the characteristic length scale and turbulence statistics, we now examine in spectral space if that also implies a modification in the range of eddy scales that contribute the most to the turbulent transport. In the frequency domain, the correlation spectrum (Wang *et al.* 2016) is defined as $R_{XY} = Co_{XY}/(\sqrt{\Gamma_X}\sqrt{\Gamma_Y})$, where Co_{XY} is the cospectrum of time series X and Y and Γ_X and Γ_Y are the power spectra of X and Y, respectively. If Y is vertical velocity fluctuations w' and X is u' or θ', R_{XY} is interpreted as a frequency specific transport efficiency (Wang *et al.* 2016). The total length of the collected time series defined in time unit L_z/U_0 is approximately 60, where U_0 is the free-stream velocity. We then section the total time series into 20 sub-series of

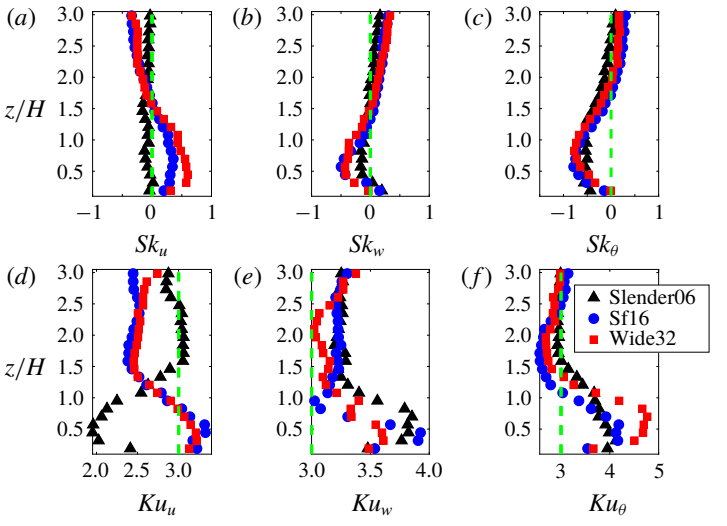

FIGURE 3. (Colour online) Skewness and kurtosis of fluctuating quantities at x_3: u' in (a,d); w' in (b,e); θ' in (c,f). Green dotted lines indicate skewness $= 0$ in (a–c) and kurtosis $= 3$ in (d–f).

equal length, and perform an ensemble average of the spectra of the 20 samples at each representative point x_i. The presence of the obstacles makes the interpretation of spectra computed from spatial fields challenging (for example they would contain the dispersive contribution), and thus we rely on time series at a given point instead. One could convert the frequency to a wavenumber using Taylor's frozen turbulence hypothesis, but this might lead to some uncertainties in the conversion (Cheng *et al.* 2017) that we prefer to avoid here. The results are shown in figure 4, where only results at x_3 (in front of the obstacle) are presented; similar conclusions can be obtained from the results at other points (not shown here).

Low-frequency eddies contribute to the efficient transport of both momentum and scalars, but a wider range of scales contribute to $R_{\theta w}$. Higher correlation spectrum values can be noted for scalars, compared to momentum, for all three cases between $10 < f\delta/u_* < 10^2$. As the roughness frontal blockage, and the streamwise distance between the elements, increase (e.g. for case Wide32), more lower-frequency motions can penetrate into the canopy more easily and they become more efficient in transporting momentum below the canopy top (figures 4*a* to 4*c*). This finding for cases with larger λ_f is consistent with the results obtained from hot-wire anemometry measurements in a wind tunnel by Perret *et al.* (2019), who noted that the canopy-induced smaller-scale motions strongly interact with the boundary-layer-scale motions. For scalars on the other hand, it seems slower motions spanning a larger range of frequency are the most efficient at transport deep inside the canopy at intermediate densities λ_f (case Sf16), becoming less efficient in case Wide32. In summary, figure 4 shows the change in time scales of the most efficient transport eddies across different geometries. As the transition to a mixing-layer-type flow indicated in figure 2 occurs, lower frequencies contribute more effectively to momentum transport in the canopy and roughness sublayer. However, for scalar transport, there seems to be an optimal configuration or density for the large scalar motions to interact effectively with the lower part of the canopy.

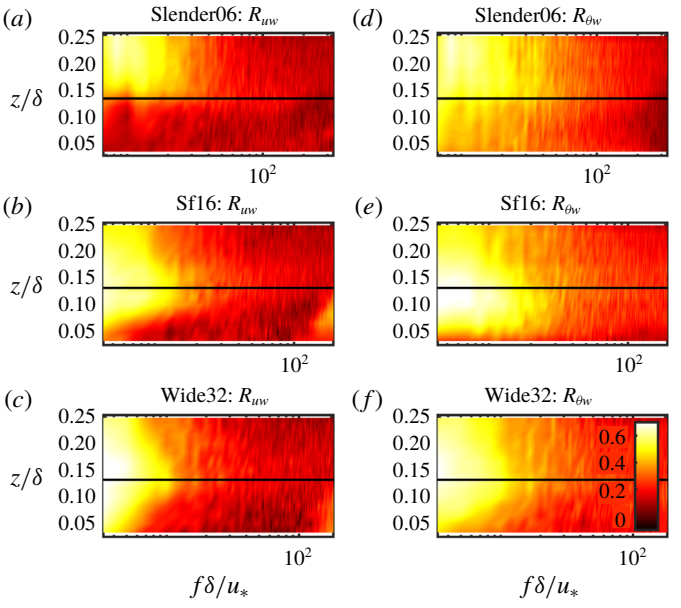

FIGURE 4. (Colour online) Pseudocolour plot of the correlation spectra R_{uw} in (*a–c*) and $R_{\theta w}$ in (*d–f*) for different cases x_3. The solid horizontal black line denotes the top of the obstacles.

The iso-surfaces of instantaneous high temperature, θ_{high}, are shown in figure 5. Here, θ_{high} is defined as $\theta + 1.5\theta_{rms}$ computed at $z/H = 1$ at any instant. We colour these iso-surfaces by the instantaneous normalized Reynolds stress and wall-normal scalar flux (figures 5*b*,*d* and 5*e*,*f*, respectively). Although both Slender06 and Wide32 demonstrate streamwise thermal 'streaks' (Hetsroni *et al.* 1999; Leonardi *et al.* 2015), Wide32 is characterized by more patchy structures in most of the domain; whereas the temperature iso-surfaces in Slender06 are more elongated in the streamwise direction and are aligned in between the staggered roughness elements.

Stronger flow disturbance by the obstacles are observed in the mixing-layer-like flow where the more obstructive three-dimensional geometry is found to significantly disrupt the structures, in agreement with the experimental observations in Hetsroni *et al.* (1999). Focusing now on the flux intensity depicted by the colours on the instantaneous flow structures, there can also be discernible dissimilarities between $w'\theta'$ and $-w'u'$ in the canopy sublayer, suggesting that some eddies might be carrying momentum but not scalars or *vice versa*. Thus, we conduct a quadrant analysis in the next section to further investigate the (dis)similarity of momentum and scalar transport.

3.1.2. *Similarity of turbulent momentum and scalar transport*

Quadrant analysis is a useful and widely used technique for probing how turbulent motions evolve and produce transport in the wall-normal direction (Wallace 2016). Thus, we apply this technique here to compare the momentum and scalar turbulent transports over the canopy and roughness sublayers. The definition of each quadrant for momentum flux follows previous studies (Katul, Hsieh & Kuhn 1997*a*; Katul *et al.* 1997*b*; Li & Bou-Zeid 2011): Q1 events are classified as $s' > 0$ and $w' > 0$;

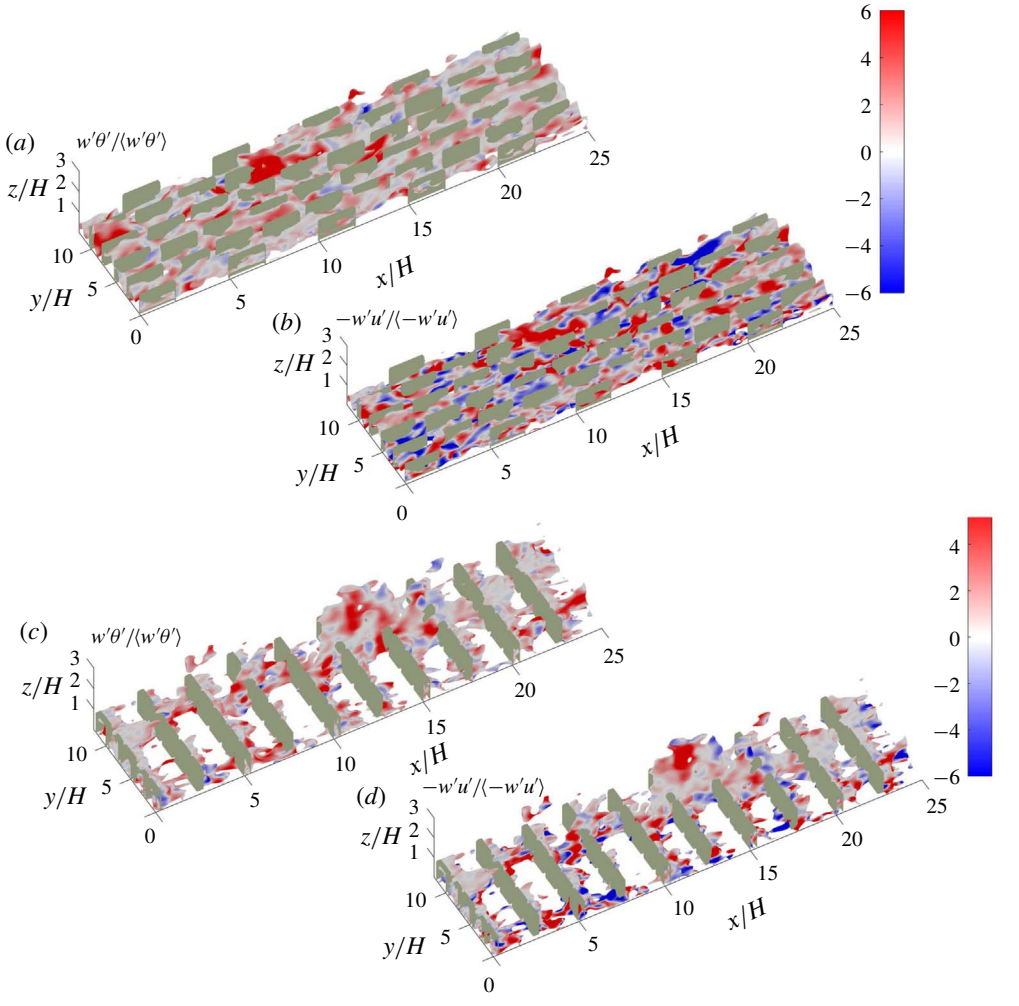

FIGURE 5. (Colour online) Iso-surfaces of θ_{high}, where $\theta_{high} = \langle\theta(z=H)\rangle + 1.5(\theta_{rms}(z=H))$ low-pass filtered for better visualization, for Slender06 in (*a*,*b*) and for Wide32 in (*c*,*d*). $\theta_{rms}(z=H)$ denotes the standard deviation of a snapshot of θ at $z=H$.

Q2 as $s' < 0$ and $w' > 0$; Q3 as $s' < 0$ and $w' < 0$; Q4 as $s' > 0$ and $w' < 0$, where s is u or θ. A prime denotes the turbulent perturbation of an instantaneous value from its Reynolds average, surrogated for here only by a time average and denoted by an overbar. We applied quadrant analysis to time series collected at the four representative horizontal locations (x_1 to x_4) indicated in figure 1 and at every height, but we will only show results for x_2 and x_3 since the other locations convey the same information (they are shown in appendix B). The same averaging procedure detailed for the results of the skewness is used here. For the momentum flux, Q2 and Q4 are termed ejections and sweeps respectively; for scalar flux, Q1 (motion that transports higher concentrations of the scalar upward, the wall being a source here) and Q3 (motion that brings lower concentrations downward) are termed ejections and sweeps, respectively. Compared to the other two quadrants, the ejections and sweeps are the dominant events in transporting momentum and scalars; they contribute to down-gradient transport.

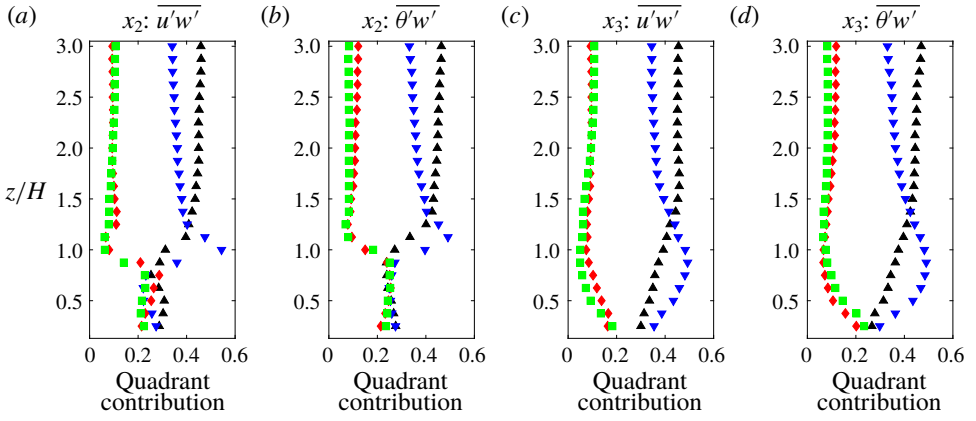

FIGURE 6. (Colour online) Contribution to total flux for (*a*,*c*) momentum and (*b*,*d*) scalar at points x_2 (back) and x_3 (front) in case Cube25. Ejections are black $\triangle$; sweeps are blue $\triangledown$; outward interactions ($w' > 0$ and $u' > 0$ or $\theta' < 0$) are red $\diamond$; and inward interactions ($w' < 0$ and $u' < 0$ or $\theta' > 0$) are green $\square$.

Figure 6 shows the contributions from various quadrants (momentum in *a*,*c*; scalar in *b*,*d*) for case Cube25, where the contribution of quadrant i is defined as $|\overline{s'w'}|_i / \sum_i |\overline{s'w'}|$. The contribution of each quadrant to scalar fluxes is broadly similar to that of momentum across all points, though slight differences between momentum and scalars are seen inside the canopy sublayer below $z/H = 1$. The spatial variation across the four different horizontal location in the canopy sublayer is on the other hand significant, underlining the complexity of the flow within these three-dimensional roughness arrays. These differences blend away above the canopy. The number of ejection events exceeds that of sweeps below $z/H = 1.25$ across all four points (not all shown here), indicating that below this height sweeping events are stronger compared to the more frequent and less intense ejections. The cross-over point at $z/H = 1.25$ is consistent with results for the Reynolds stress from DNS reported by Coceal *et al.* (2007*a*) for the same underlying roughness geometry of staggered cubes, although they averaged over all points at a given z. It has been previously observed that for momentum transport the sweeps' contribution to total stress dominates over ejections in the neutral roughness sublayers of vegetation canopies (Dupont & Patton 2012) and in a realistic urban area characterized by large roughness elements (Rotach 1993; Christen, van Gorsel & Vogt 2007). Dominance of sweeps in momentum transport over very rough walls, compared to the dominance of ejections over smooth and less rough counterparts, is in general agreement with the picture proposed and discussed in detail by Raupach, Finnigan & Brunei (1996) who adopted a mixing-layer analogy for these very rough walls to account for the differences compared to typical flows over smooth or small-roughness walls. In the outer layer, the dominance of ejections is restored as typical in smooth-wall boundary layers (Adrian 2007).

Our results for case Cube25 demonstrate that the turbulent transport of a passive scalar exhibits similar behaviour to momentum. Similarity or dissimilarity between momentum and passive scalar transport over wall-bounded turbulent flows has also been discussed in the literature. For instance, similarity in the transport is found in laboratory results (Perry & Hoffmann 1976; Nagano & Tagawa 1988) over smooth surfaces and field measurements in the atmospheric boundary layer over

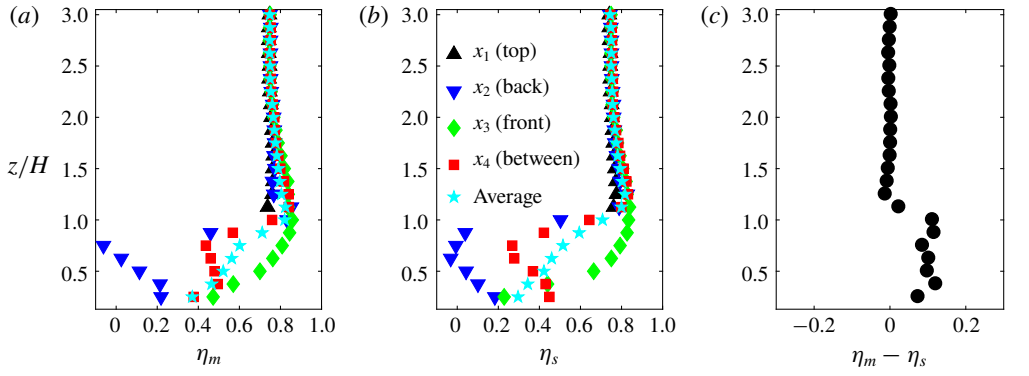

FIGURE 7. (Colour online) Turbulent transport efficiencies at x_1–x_4 for the case of staggered cubes. (*a*) Momentum transport efficiency η_m; (*b*) scalar transport efficiency η_s; (*c*) $\eta_m - \eta_s$ averaged over points x_1–x_4.

vegetation canopy and in the roughness sublayer over an urban area (Dupont & Patton 2012; Wang *et al.* 2014), and in DNS over two-dimensional square-shaped obstacles (Leonardi *et al.* 2015). Dissimilarity is not as extensively reported (Christen *et al.* 2007), except when buoyancy begins to play a significant role in turbulence generation (Li & Bou-Zeid 2011). The generalizability of the similarity between turbulent transport of momentum and scalar observed above for case Cube25 to other cases is assessed through quadrant-analysis-based turbulent transport efficiencies, defined as $\eta = F_{total}/(F_{ejection} + F_{sweep})$ (Wyngaard & Moeng 1992; Li & Bou-Zeid 2011), where F is the (total or from a single quadrant) flux of momentum or scalars. The results for cases Cube25, Slender06 and Wide32 are shown in figures 7–9. Figures 7–9(*a*,*b*) show the vertical profiles of efficiencies at each of the four horizontal locations x_1 to x_4, as well as an average over these points, while figures 7–9(*c*) show the difference between η_m and η_s, averaged over the four points.

Above $z/H = 1.25$, $\eta_m - \eta_s$ approaches 0 and spatial variability is blended out at all points and across all cases shown in figures 7–9. Below that blending height, case Cube25 (figure 7) shows the most significant spatial variation of efficiencies across the four points; η_m and η_s for Slender06 (figure 8) vary much less while for Wide32 the efficiencies deviate appreciably only at x_4. We need to note however that these locations and their relative distance are not all equivalent since their locations relative to the cuboids are not identical in all cases.

Although there are some discrepancies between η_s and η_m at some locations, such as at x_2 and x_4 within the canopy sublayer of Cube25 and Wide32, the general trends for momentum and scalar efficiency remain similar for those cases. On the other hand, Slender06 displays more dissimilarity between momentum and scalar transport in the canopy sublayer as shown by the η values (figure 8), with a higher transport efficiency for the scalar. While sweeps dominate the transport of the scalar in Slender06 (figure 18), both sweeps and ejections contribute approximately equally to the total momentum flux (figure 17), especially at points x_3 and x_4. A physical explanation for this dissimilarity is that the penetration of high horizontal momentum sweeps downward is hindered by the blockage effect of the slender-shaped roughness element, which induces negative fluctuations in u' and thus increases inward interactions and reduces η_m. Nevertheless, sweeps that are associated with cold (low θ') fluid, but not with a large positive u', can still efficiently penetrate the canopy and transport the

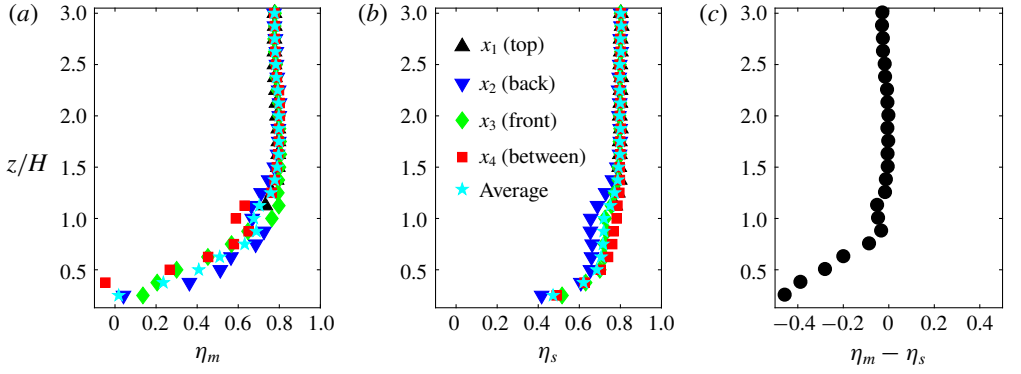

FIGURE 8. (Colour online) Same as figure 7, but for case Slender06.

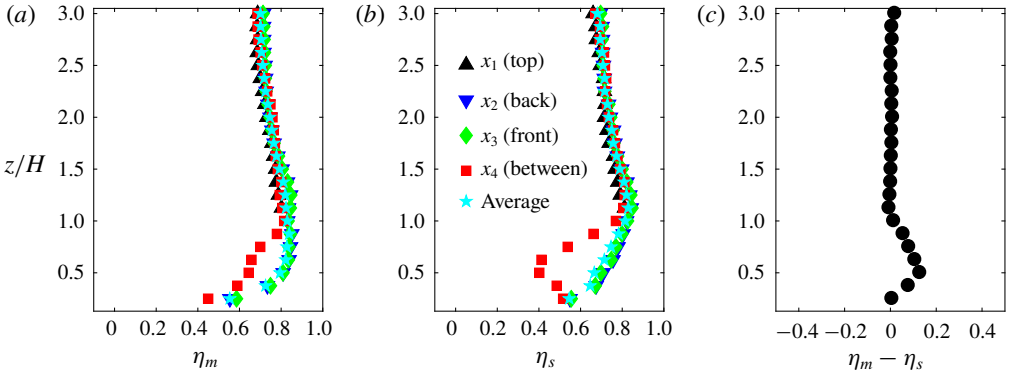

FIGURE 9. (Colour online) Same as figure 7, but for case Wide32.

passive scalar. Overall, turbulent momentum and scalar transport are broadly similar for Cube 25 and Wide 32, but not for Slender06 that has a higher η_s than η_m.

It would be instructive to analyse further why the slender blocks induce more dissimilarity than the wider ones, but this is not a core goal of this paper and will not be pursued here. What we can conclude is that, as the general characteristics of turbulent flows transitions from wall-bounded-like to a mixing-layer-like regime, u' and θ' exhibit more similar correlations with w'. For these mixing-layer-like flows, turbulent momentum and scalar transports are broadly similar but with a slightly more efficient momentum transport ($\eta_m > \eta_s$). However, this similarity is reduced for wall-bounded-like flows and the more efficient exchange is now for scalars ($\eta_m < \eta_s$) when measured using quadrant analysis (note that for the efficiency defined based on the correlation coefficient in figure 2, momentum transfer remained slightly more efficient than scalar transfer for the slender geometry). For all geometries, the results suggest a turbulent Schmidt or Prandtl number $\neq 1$ (results not shown here).

3.1.3. *Velocity and passive scalar structures*

To understand how turbulent momentum and scalar transport behave as the flow regime transition illustrated in the previous sub-section occurs, we analyse the spatial correlations of turbulent quantities. The two-point streamwise correlation for

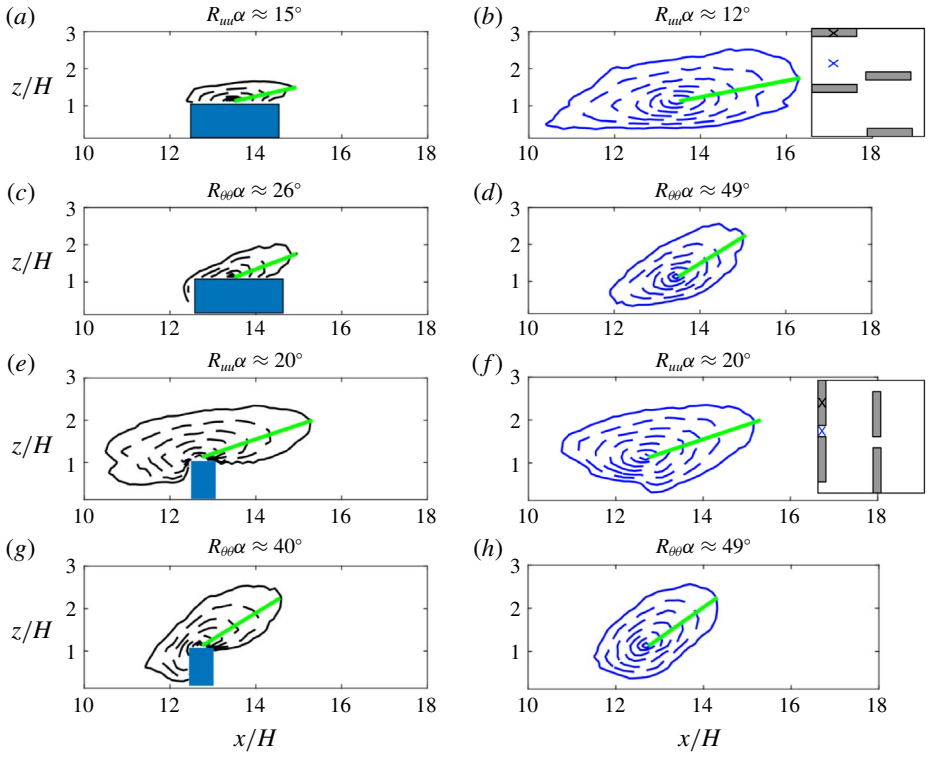

FIGURE 10. (Colour online) Two-point streamwise correlation for u and θ for case Slender06: (*a–d*) and case Wide32: (*e–h*). The black (blue) crosses in the inset figures (in *b*,*f*) indicate the reference points X_0 in figures *a*,*c*,*e*,*g* (*b*,*d*,*f*,*h*). The black (blue) crosses are positioned at the middle of the top of the cuboids and between the cuboids respectively. The correlation contours are spaced uniformly with a step 0.1 from 1 (innermost) to 0.3 (outermost). The solid green line segments are drawn between X_0 and X_1, where X_1 is on the furthest point on the correlation contour of 0.3. The angle α is between the streamwise direction and the line segment X_0X_1.

a quantity s at reference point x and for a separation distance X_0 can be computed as $\overline{\rho_{ss}}(X_0, x) = \overline{s'(X_0)s'(x)}/(s_{rms}(X_0)s_{rms}(x))$, where r.m.s. denotes the root mean square of the turbulent fluctuations. These correlations are shown in figure 10 for cases Slender06 and Wide32. The angle of inclination of the contours was calculated following the approach of Leonardi *et al.* (2015), where α is estimated as the angle between the horizontal direction and the segment X_0X_1, indicated by the green solid line, the point X_1 being the furthest from X_0 on the contour $R_{uu} = 0.3$. The increased interactions between the roughness elements and the flow in the roughness sublayer are indicated by larger α, especially $R_{uu}(x_2)$ in figure 10(*f*) relative to figure 10(*b*). Compared to the two-dimensional bars studied in Leonardi *et al.* (2015), the three-dimensional roughness geometry and different configurations also introduce spanwise variation in the correlation contours. The mixing-layer-like flow regime results in increased interactions between the surface and the roughness sublayer for both u' and θ'. However, the increase is more pronounced for the velocity and the correlation contours $R_{\theta\theta}$ are less sensitive to the increase of λ_f than their velocity counterparts.

Nevertheless, the angles for θ' are always larger than for u'. Even for a surface-layer-like flow regime of the slender geometry, where the coupling between canopy sublayer top and the roughness sublayer aloft is not as strong as that for the mixing-layer-like case, the effect of the roughness geometry on a passive scalar can extend further up. This result is also consistent with the lower frequency (larger scale) of the motions contributing to $R_{\theta w}$ than to R_{uw} in figure 4, as well as with the wider range of scales that can effectively transfer scalars as deduced from the spectral analysis. It should be noted here that this analysis is restricted to a plane that crosses the buildings, and indicates longer coherence for the wide, more obstructive geometry. Most of the coherent structures for the slender geometry are in between the buildings as illustrated in figure 5 and would not be captured in this correlation coefficient analysis.

3.2. *Dispersive transport*

An important aspect that sets very rough walls apart is that dispersive stresses or fluxes, which arise from the spatial inhomogeneity of the time-averaged flow field, can be important contributors to total transport (Wilson & Shaw 1977; Finnigan 1985, 2003). Any mean (time-averaged) quantity $\overline{\phi}$ can be decomposed into $\overline{\phi} = \langle\overline{\phi}\rangle + \overline{\phi}''$, where the double prime represents the spatial deviation of the time-averaged variable from its time–space average. In the present paper, we consider $\langle\overline{\phi}\rangle$ representing the planar average of a time-averaged quantity over the volume of $\mathrm{d}zL_xL_y$ (i.e. a planar average). The dispersive fluxes then arise from the spatial averaging of (2.2) and (2.3). As an example, the spatially local, time-averaged dispersive momentum stress is $\overline{u}_i''\overline{u}_j''(x, y, z)$. Taking the volume averaging over $\mathrm{d}zL_xL_y$, $\langle\overline{u}_i''\overline{u}_j''\rangle(z) = \langle\overline{u}_i\overline{u}_j\rangle - \langle\overline{u}_i\rangle\langle\overline{u}_j\rangle$. Physically, the dispersive stresses result from the transport by the mean (time-averaged) coherent flow structures, such as the persistent circulations that will form between buildings.

3.2.1. *Dissimilarity between dispersive momentum and heat transport*

Figure 11 shows the ratios $F_{dis}/F_{total} = \langle\overline{u}''\overline{w}''\rangle/(\langle\overline{u}''\overline{w}''\rangle + \langle\overline{u'w'}\rangle)$ and $F_{turb}/F_{total} = \langle\overline{u'w'}\rangle/(\langle\overline{u}''\overline{w}''\rangle + \langle\overline{u'w'}\rangle)$ in (*a*) and their counterparts $\langle\overline{w}''\overline{\theta}''\rangle/(\langle\overline{w}''\overline{\theta}''\rangle + \langle\overline{w'\theta'}\rangle)$ and $\langle\overline{w'\theta'}\rangle/(\langle\overline{w}''\overline{\theta}''\rangle + \langle\overline{w'\theta'}\rangle)$ in (*b*) for all the cases with $\lambda_p = 0.12$ and for increasing λ_f (Slender06 to Wide32). Examples of previous studies on the momentum dispersive fluxes (Christen & Vogt 2004; Poggi *et al.* 2004; Martilli & Santiago 2007; Coceal, Thomas & Belcher 2007*b*; Poggi & Katul 2008; Leonardi *et al.* 2015; Giometto *et al.* 2016) and a few on dispersive scalar fluxes (Christen & Vogt 2004; Leonardi *et al.* 2015) have demonstrated their importance within the canopy sublayer, as well as in the roughness sublayer. Similar to previous findings, our simulations also indicate that the dispersive fluxes are significant within the roughness arrays. The dispersive flux can contribute $\approx$50 % of the total momentum or scalar flux (where the contribution of the subgrid-scale fluxes is included in the total) below the roughness elements height for some cases. It is noteworthy that there are no monotonic trends of how the dispersive fluxes vary with λ_f, reflecting the complexity of how the mean circulations change with changing geometry. The fractions of dispersive fluxes, in general, are the highest for the most eccentric geometries Slender06 and Wide32. Our results show that for $z/H = 2$–3 dispersive fluxes for most cases are close to zero, broadly in agreement with Coceal *et al.* (2007*a*) and Leonardi *et al.* (2015). We performed our analysis for the time-averaged quantities over time spans of approximately $H/U_b = 1200$ (U_b is the bulk velocity) and longer than the $H/U_b = 600$ suggested in Leonardi

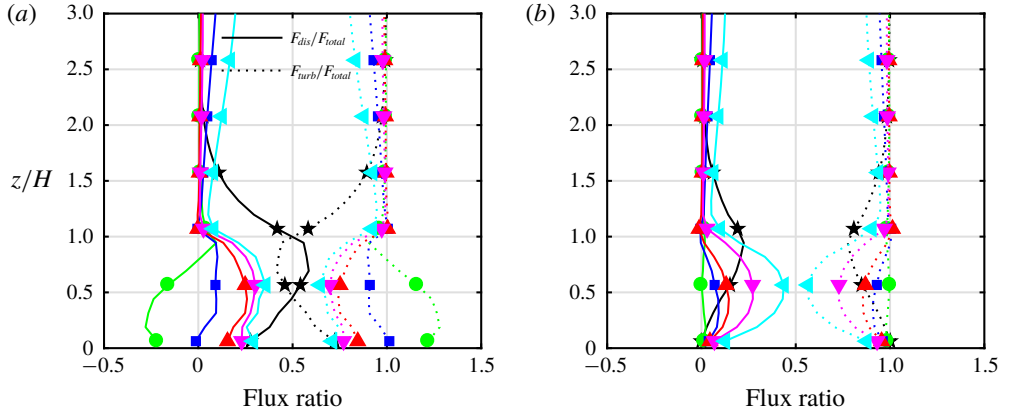

FIGURE 11. (Colour online) Contribution of x–y-averaged dispersive or turbulent (resolved + subgrid-scale) fluxes to the total for (a) momentum and (b) scalar. ★, Slender06; ○, Sf08; □, Sf12; △, Sf16; ▽, Sf24; ◁, Wide32.

et al. (2015), who found that such an averaging time is required for secondary non-persistent circulations in the roughness sublayer to meander and be transported away.

Both dispersive stress and scalar flux are important portions of the total fluxes especially within the canopy sublayer, and their dissimilarities are now studied in detail. Figure 12 shows $\overline{u}''_N = \overline{u}''/\langle u(z=H)\rangle$ and $\overline{\theta}''_N = \theta''/\Delta\theta$, where $\Delta\theta = \langle\theta(z=H) - \theta(z=0.125H)\rangle$ for an x–z cross-section indicated by the blue line in figure 1. The pseudocolour plots and streamlines are phase averaged for all repeating units in the domain. Negative $\overline{u}''_N$ is due to loss of horizontal momentum u in the wakes produced by the obstacle, as well as due to upstream blockage as the flow approaches a block. Positive $\overline{\theta}''_N$, on the other hand, are prominent only in the lee of obstacles and result from all three canyon surfaces (ground and walls) being kept at a higher temperature. As λ_f increases, in figures 12($b1$) to ($f1$) and 12($b2$) to ($f2$) the most pronounced momentum–scalar distinction can be found upstream of the obstacle where the mean recirculation pattern results in 'counter-gradient' dispersive momentum transport (fluid slowed by the pressure field generated by the obstacle being advected downwards) but 'down-gradient' scalar transport (cooler or lower concentration fluid transported downwards). This difference emerges from the non-local action of pressure on momentum (the fluid's streamwise velocity has to decrease as it approaches the windward face even before it contacts that face), but its absence from the dynamics of scalars (the fluid has to 'touch' the surface to uptake scalars). The sign of the dispersive scalar fluxes in that region is thus the same as the total flux, while there is partial cancellation of dispersive stresses for momentum. As λ_f increases, the region that contributes to 'down-gradient' dispersive flux enlarges, especially from Slender06 to Sf24. Case Slender06 generates a mean flow that is fundamentally different from the other geometries since flow separation and the emergence of a (resolved) recirculation zone behind the obstacle only starts with case Sf08. In addition, upstream of the obstacle, a downward flow appears in case Sf08, resulting in downward transport of colder air (green region near $x/H = 5$). However, such downward flow upstream of the building is absent in Slender06.

Due to the asymmetry of the obstacles in the x and y directions, isolating the spatially coherent characteristics of the dispersive fluxes in each direction can inform

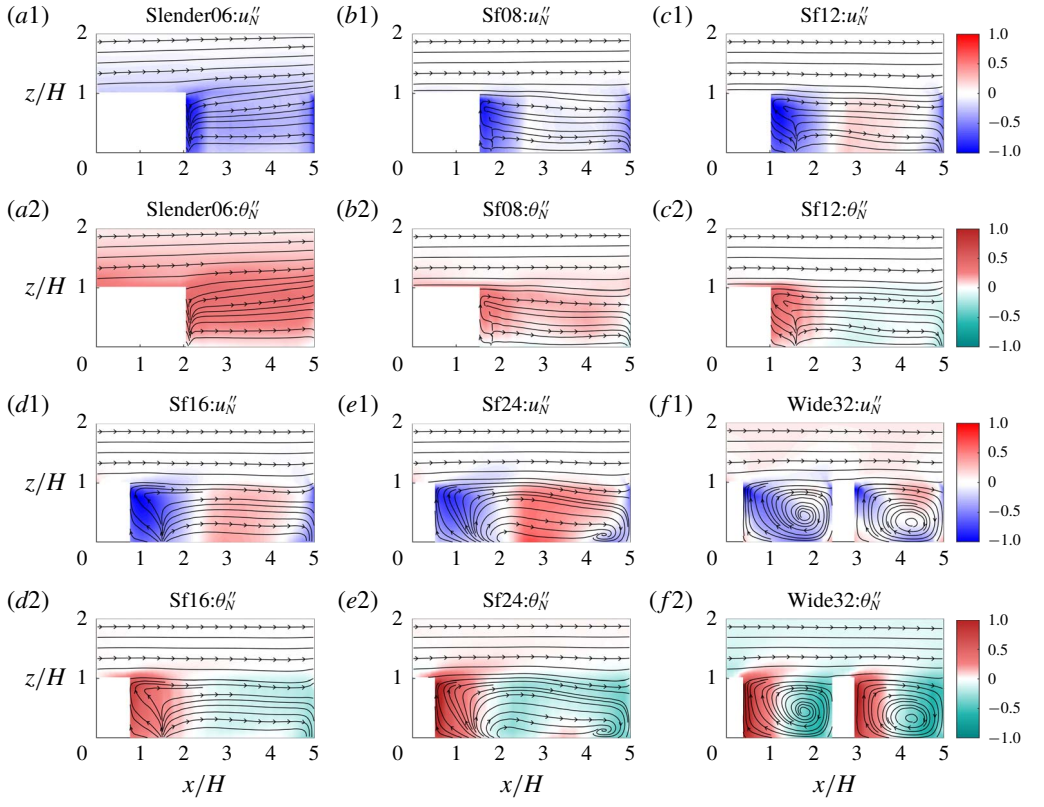

FIGURE 12. (Colour online) Normalized dispersive stress and flux for all cases: colour scale indicates $\overline{s}_N'' = \overline{s}''/\Delta s$ for $s = u$ or θ. Lines with arrows are the $\overline{u}$–$\overline{w}$ streamlines.

us of the direction-specific variabilities of the temporally averaged quantities. To probe this aspect, we first define the deviation of a temporally averaged quantity, $\overline{\phi}$, from a direction-specific spatial average $\langle\overline{\phi}\rangle_i$:

$$\overline{\phi}_i'' = \overline{\phi} - \langle\overline{\phi}\rangle_i, \tag{3.1}$$

where $\langle\rangle_i$ denotes the average over the ith direction. The direction-specific dispersive fluxes averaged in the same direction $\langle\overline{s}_i''\overline{w}_i''\rangle_i$ physically represent the magnitude of spatial covariance, or the dispersive contribution linked to variability, in the i-direction alone. These fluxes will vary in the other horizontal direction, but can then be averaged in that direction; for simplicity, we denote the planar-averaged direction-specific dispersive fluxes as $\langle s''w''\rangle_i$. The results are shown in figure 13 normalized by the total flux $(\langle\overline{s}''\overline{w}''\rangle + \langle\overline{s'w'}\rangle)$, where s is u or θ. We reiterate that, compared to the regular dispersive fluxes, direction-specific dispersive fluxes inform us about how the spatial variability in each direction contributes to the spatial covariance. Therefore, it is noteworthy that the dissimilarities between the dispersive transport of momentum and scalar are observed in both x and y directions. Figure 13(b) clearly depicts a monotonically increasing $\langle\theta''w''\rangle_X$ with λ_f, but the 'cancellation' effect leads to non-monotonic variation of $\langle u''w''\rangle_X$ with λ_f (figure 13a). An equally important aspect of the results is that the x-variability is more important than the y-variability

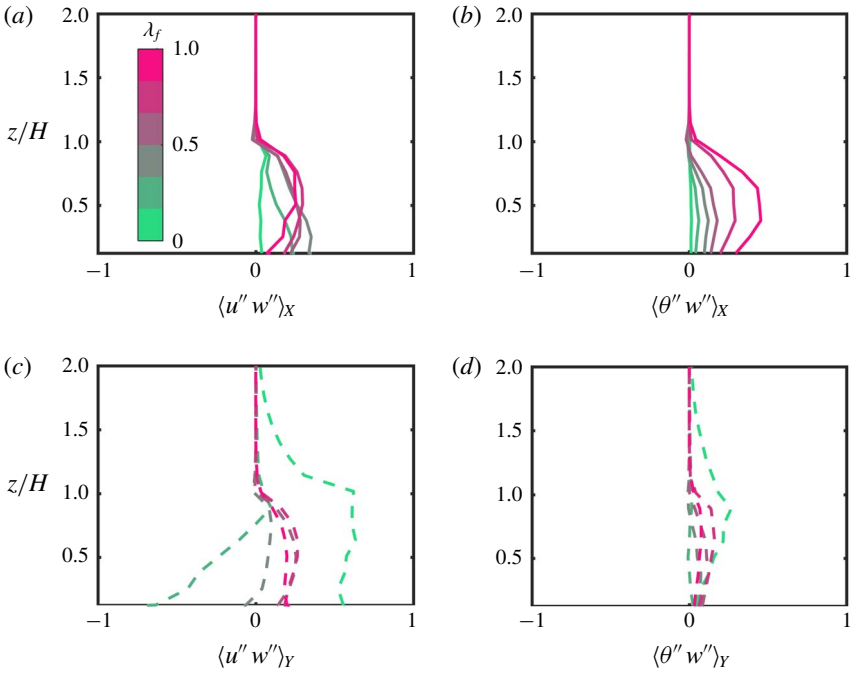

FIGURE 13. (Colour online) Normalized direction-specific dispersive stress and flux for all cases: colour scale indicates λ_f, subscripts X or Y indicate direction-specific fluxes in the streamwise or spanwise direction (both subsequently planar averaged). (*a*,*c*) Streamwise and spanwise direction-specific normalized momentum stresses, respectively; (*b*,*d*) streamwise and spanwise direction-specific scalar fluxes, respectively.

for the wider geometries, and the reverse is true for slender ones, as expected. For the y-specific dispersive momentum stress, Slender06 stands out as the case that is completely dominated by this component (figure 13*c*). This also applies to scalar fluxes, although there is less variation with geometry. This underlines the role of the long streamwise rolls that form in between the obstacles in case Slender06 (depicted in figure 5) and that seem to be significantly weakened even by the slight widening of the obstacles in Sf08.

3.2.2. *Effects of geometry on dispersive transport efficiency*

The effects of different geometries on the dispersive fluxes can be further studied using the approach of quadrant analysis, but now applied to $\overline{u}''$, $\overline{w}''$ and $\overline{\theta}''$ (Pokrajac *et al.* 2007; Poggi & Katul 2008) in a similar way to applying it to turbulent fluctuations. Instead of indicating the presence of turbulent events, each quadrant event reveals the spatially coherent structures of the time-averaged quantities. An equivalent dispersive transport efficiency can be defined as the ratio of the total flux $\langle \overline{u}''\overline{w}'' \rangle(z) = \sum_i^4 F_i$ to the sum of the two F_i contributions producing down-gradient fluxes. Here F_i is the dispersive flux contribution of the ith quadrant $F_i(z) = (L_x L_y)^{-1} \int_A I_i(x, y, z)\overline{u}''(x, y, z)\overline{w}''(x, y, z)\mathrm{d}A$, where I_i is an indicator function of the quadrant event and A is extent of the horizontal domain. The same sign convention as the turbulent fluctuating components is applied to $\overline{u}''$, $\overline{w}''$ and $\overline{\theta}''$. The transport efficiency for momentum (η_m^d) and scalars (η_θ^d) for the dispersive fluxes

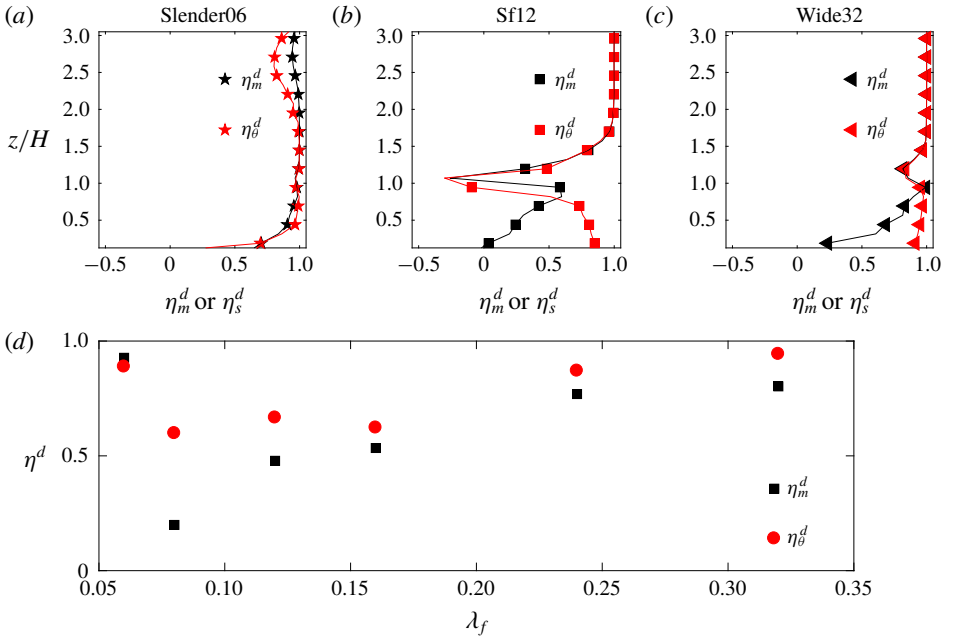

FIGURE 14. (Colour online) Dispersive transport efficiencies for different cases: (*a*) ★, Slender06; (*b*) □, Sf12; (*c*) △, Wide32; (*d*) η_m^d and η_θ^d averaged for $0 \leqslant z \leqslant 2H$.

is hence defined as $\eta = \sum_i F_i / \langle F_2 + F_4 \rangle$. For instance, when $u'' < 0$ and $w'' > 0$, we denote it as a dispersive 'sweep', which indicates a persistent spatial feature. Similarly, we can also define a direction-specific dispersive transport efficiency for $\langle \overline{s}_X'' \overline{w}_X'' \rangle$ and $\langle \overline{s}_Y'' \overline{w}_Y'' \rangle$ as η_X^d and η_Y^d, respectively.

Figure 14(*a–c*) indicates that there is distinct dissimilarity between the vertical distribution of η_θ^d and η_m^d, related to the physical differences that arise from the role of pressure discussed above. In general, $\eta_m^d < \eta_s^d$, except for case Slender06 shown in figure 14(*d*). This is in stark contrast to the turbulent transport efficiencies shown in figure 7 where the slender case was the one showing a lower turbulent momentum transport efficiency. As λ_f increases, a non-monotonic trend is observed for the difference between 'efficiency' of dispersive transport of momentum and the passive scalar, with the most eccentric geometries again showing the highest transport efficiencies. The high efficiency in Slender06 can be understood as a result of the absence of the 'cancellation' effect as discussed in the previous paragraph, and of the stronger dispersive variability in the lateral direction as indicated in figure 13(*c*) and by the long structures depicted in figure 5. The lower pressure drag associated with the small λ_f in Slender06 prevents the formation of a recirculation zone and no 'counter-gradient' dispersive momentum flux at the leading edge is present. With increasing λ_f, the y-direction dispersive fluxes drop, even becoming negative for the Sf08 momentum flux (figure 13*c*) due to strong 'counter-gradient' fluxes at the leading edge. As λ_f continues to increase, the influence of the y-direction variability is minimized and the x-direction dominates, resulting in a monotonic increase in the efficiency as the 'down-gradient' dispersive momentum fluxes in the recirculation region increase. Therefore, a number of competing factors, such as the differences in spatial variabilities in x and y directions for different geometries, collectively influence the non-monotonic behaviour of dispersive fluxes as λ_f increases.

Dispersive transfer of scalar is less impacted by the change of geometry due to the absence of cancellation effect. However, with larger recirculation regions (from cases Sf08 to Wide32), the efficiency and magnitude of both the dispersive momentum and scalar fluxes are enhanced. The complex flow dynamics and non-monotonic changes with λ_f underline the need for more detailed investigation to relate the universal features of dispersive transport of momentum and scalar to the topological characteristics of the surface, and to construct a model for dispersive fluxes. However, since this is not one of the central research questions of this study, we have to leave it to future investigations.

4. Conclusion

We use LES to compare and contrast the transport of momentum and passive scalars, by turbulent and dispersive fluxes, over very rough surfaces consisting of three-dimensional cuboidal roughness elements. The focus is on the canopy and roughness sublayers, since above these layers the flow reverts to a canonical wall-bounded flow regime. The effect of the frontal blockage of the roughness geometry on the fluxes is also investigated.

The influence of different three-dimensional roughness elements alters the general turbulent flow characteristics. We observe a general transitioning behaviour from a canonical wall-bounded flow type to a mixing-layer-like one or 'obstructed shear flow', when the frontal area ratio λ_f increases. This ratio encodes the flow blockage by the roughness elements, and the preponderance of free-shear wakes behind the roughness elements. This is particularly illustrated by the decrease in the shear length scale and the enhanced penetration of low-frequency eddies (associated with large scales) into the canopy layer as λ_f increases. This transition causes a monotonic and significant increase in the momentum transport efficiency as the flow becomes more mixing layer like, while on the contrary the transport efficiency for scalars measured by the correlation coefficient changes more mildly and non-monotonically with increasing λ_f. This is mainly a result of the distinct contributions from large-scale motions in the roughness sublayer, which are able to increase the interaction between the canopy sublayer and the roughness sublayer more effectively for momentum than for scalars as the geometry is modified to increase flow obstruction. Turbulent transports of momentum and passive scalar are found to be broadly similar in general, as evidenced by a quadrant analysis, with a marginally higher averaged turbulent momentum transfer efficiency. The unique exception is case Slender06, where the difference in turbulent momentum and scalar transports becomes more substantial.

A distinct feature of flows over very rough surfaces is that dispersive fluxes can be significant, particularly for the most eccentric geometries (Slender06 and Wide32) where they amount to $\approx 50\,\%$ of the total flux. The dispersive momentum and scalar fluxes show more pronounced differences than their turbulent counterparts. Directional analysis of dispersive fluxes also confirm such differences in both the streamwise and spanwise directions, the latter displaying a higher sensitivity to the underlying surface topology. The differences between momentum and scalar dispersive fluxes are traced back to the non-local action of pressure in the momentum dispersive contributions, and the absence of a pressure counterpart for scalar transport. Thus, the geometry has a larger influence on the momentum fluxes than on the scalar fluxes, as indicated by more pronounced changes in momentum dispersive transport efficiency. The most pronounced discrepancies between momentum and scalars are noted for the more symmetric geometries, while the most eccentric ones display comparable transport

efficiencies. In particular, Slender06 again emerges as the exception, displaying the strongest scalar–momentum similarity for the dispersive part. This unique behaviour of Slender06 is shown to be related to the dominance of dispersive variability in the cross-stream direction; however, more research is needed to fully elucidate how the asymmetry of roughness elements influences the spatial coherence of the dispersive fluxes.

Although we only simulated flows with constant scalar concentration boundary conditions, the results about dis(similarity) between turbulent and dispersive fluxes and between momentum and scalars should hold for flux or mixed boundary conditions as well. On the other hand, if the scalar concentration influences buoyancy (e.g. with large temperature fluctuations), the active role of the scalars will then have a strong impact on the dynamics (Li & Bou-Zeid 2011) and the present results will be altered. This study demonstrates that the (dis)similarity between momentum and scalar transport in three-dimensional very rough surfaces can be complicated by the spatial variability of the roughness elements and the specific topology of the underlying geometry. However, the present findings, especially the significance of the scalar dispersive flux contributions over dense canopy, can inform the interpretation of experimental measurements, which are often pointwise data where dispersive fluxes cannot be estimated: such measurement in the canopy and roughness sublayers are missing nearly half of the total fluxes. This can be overcome by collecting data (e.g. using movable hotwires or particle image velocimetry) at various spatial locations to be able to assess the dispersive contributions. In addition, in the dense canopy sublayer, the mechanistic difference (arising from the pressure term) in generating dispersive momentum and scalar fluxes need to be incorporated in model development. Current parameterizations either neglect dispersive fluxes or do not distinguish them from turbulent fluxes, but, as our analyses show, their physics are quite distinct and this difference is not the same for momentum and scalars.

Acknowledgements

This work was supported by the NOAA-Princeton Cooperative Institute for Climate Science and by the U.S. National Science Foundation's Sustainability Research Network Cooperative Agreement 1444758 and grant 1664091. The simulations were performed on the supercomputing clusters of the National Center for Atmospheric Research through projects P36861020 and UPRI0007. The authors would like to thank the anonymous reviewers for their constructive comments.

Appendix A. Resolution test

A sensitivity test is carried out to examine the effect of the number of points used in representing the obstacles. It was found previously by Tseng *et al.* (2006) that at least 6 points per dimension of the obstacle are required to represent a solid in LES (they used a similar approach and LES code to the ones we are using here). Therefore, we doubled the resolutions for the case Wide32 listed in table 1. In addition, a test case with all other parameters maintained the same as Wide32 except for L_x/δ, which was doubled to 6.25, was also conducted. Figure 15 shows the comparison between the original simulation, the higher resolution case and the case with longer domain length, where θ_1 is $\langle\theta\rangle$ at $z=\delta$ and θ_0 is $\langle\theta\rangle$ at $z=1/8H$. Both test cases were run for approximately 30 eddy turnover times and are averaged for the last 15 eddy turnover times. We compute the height-averaged relative mean square error defined as $r_e^n=\langle\sqrt{(q_n-q_0)^2}/q_0\rangle_z$, where q_n is some quantity for comparison in case n ($n=1$

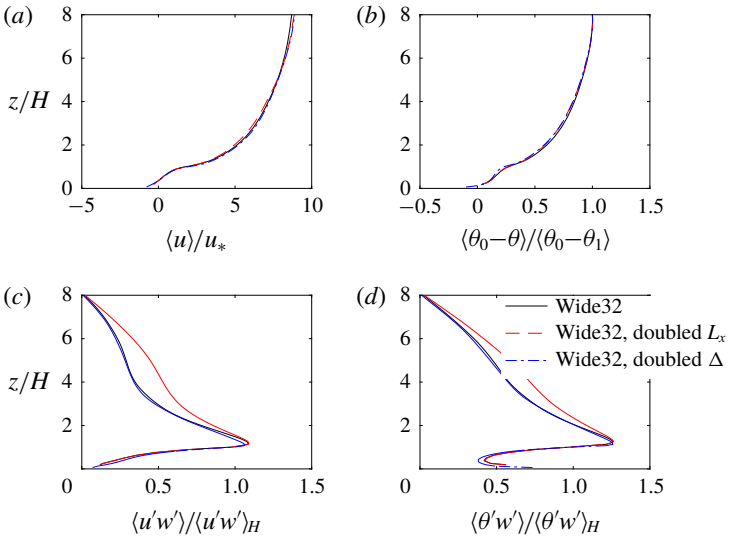

FIGURE 15. (Colour online) Comparisons of horizontally averaged quantities. (*a*) $\langle u/u_* \rangle$, (*b*) $\langle(\theta_0 - \theta)/(\theta_0 - \theta_1)\rangle$, where $\theta_0 = \theta(z = 0.125H)$ and $\theta_1 = \theta(z = \delta)$, (*c*) $\langle u'w'/u_*^2 \rangle$, (*d*) $\langle \theta'w'/u_*\theta_1 \rangle$.

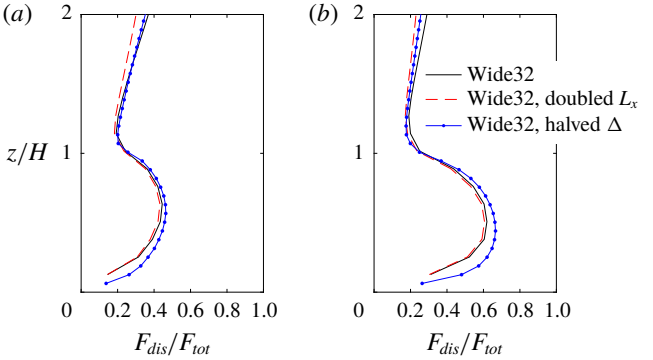

FIGURE 16. (Colour online) Comparison of the dispersive fluxes contributions for different simulation set-ups for (*a*) momentum, (*b*) scalar.

being doubled L_x and $n = 2$ being the case of double resolution in all directions) and q_0 is that same quantity from the initial set-up of case Wide32. The value of r_e^1 in percentage for (*a–d*) are 1.7, 1.5, 15 and 27 %; r_e^2 in percentage for (*a–d*) are 1.7, 2.0, 5.5 and 4.2 %. r_e^2 are all within 6 % compared to case Wide32, which shows that we achieve good grid convergence. The larger deviation seen in case of doubled L_x in the second-order moments is due to the fact that in the larger domain the streamwise roll are less persistent and the convergence to a linearly decreasing stress (as expected) is faster. However, for $z/H < 2$, the deviation in the case of doubled L_x is small, likely because of the dominance of the small-scale wall-attached eddies.

Figure 16 shows the percentage of dispersive momentum and scalar flux to total flux for these three cases. Good agreements between the three cases confirm that the differences observed between dispersive momentum and scalar fluxes are robust, especially for the roughness sublayer, which is the focus of this study.

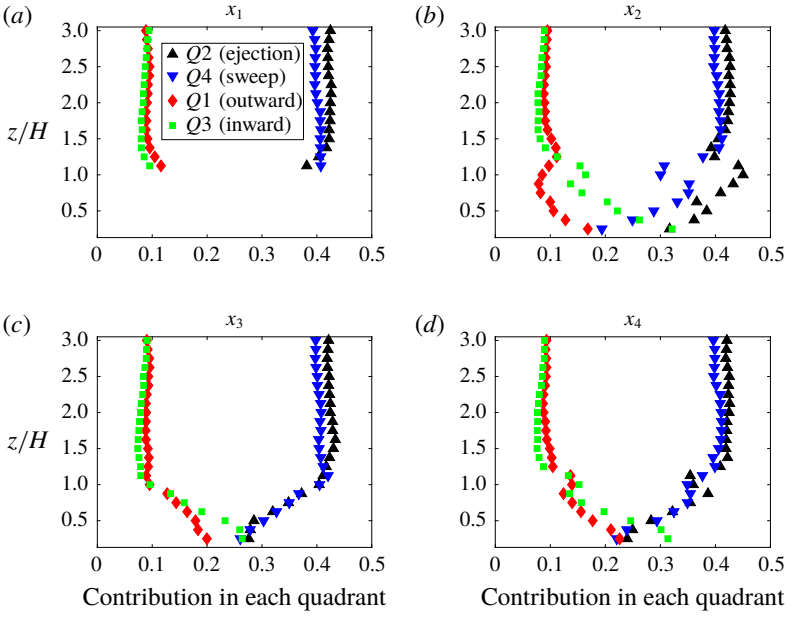

FIGURE 17. (Colour online) Contribution to total flux for momentum for Slender06. (*a–d*) points $x1$–$x4$ indicated in figure 1. Ejections are black △; sweeps are blue ▽; outward interactions are red ◇; and inward interactions are green □.

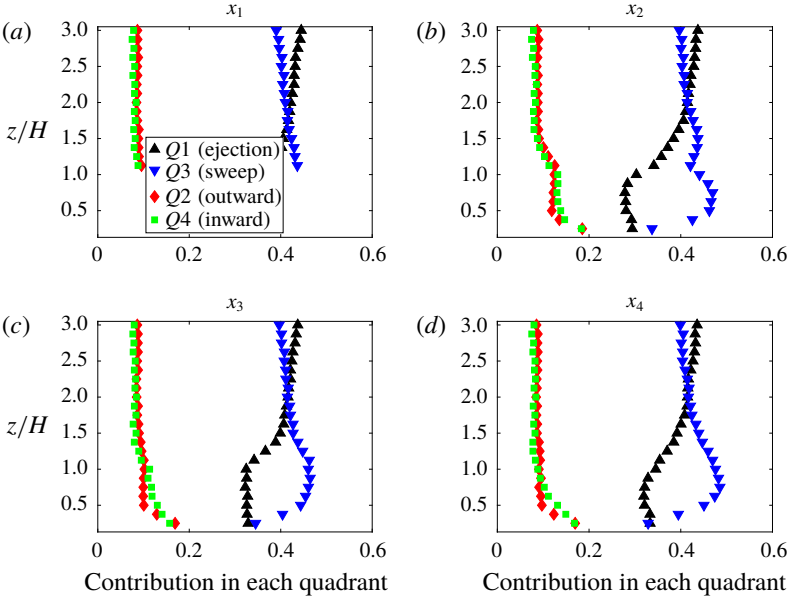

FIGURE 18. (Colour online) Contribution to total flux for scalar for Slender06 (*a–d*) points $x1$–$x4$ indicated in figure 1. Ejections are black △; sweeps are blue ▽; outward interactions are red ◇; and inward interactions are green □.

Appendix B. Quadrant analysis at different points

Quadrant analyses similar to results in figure 6 are presented here for Slender06 in figures 17 and 18; Wide32 in figures 19 and 20.

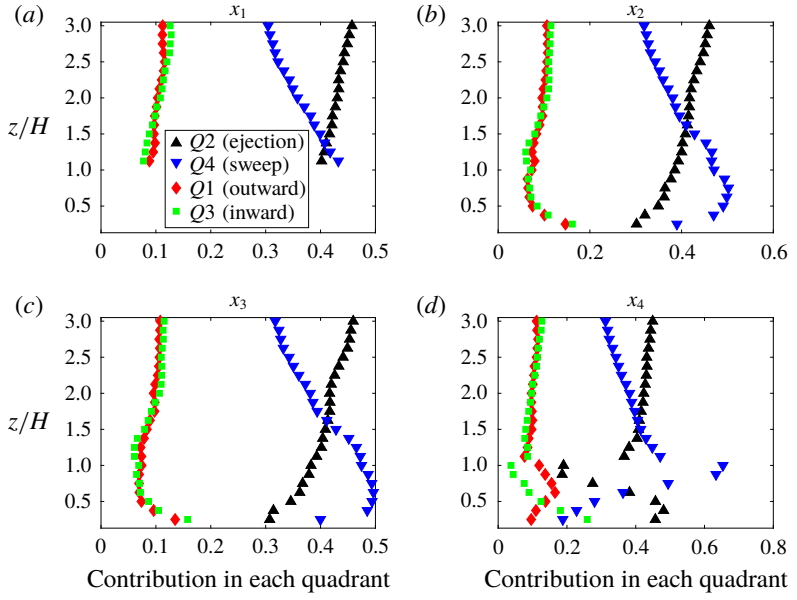

FIGURE 19. (Colour online) Contribution to total flux for momentum for Wide32 (*a–d*) points $x1$–$x4$ indicated in figure 1. Ejections are black △; sweeps are blue ▽; outward interactions are red ◇; and inward interactions are green □.

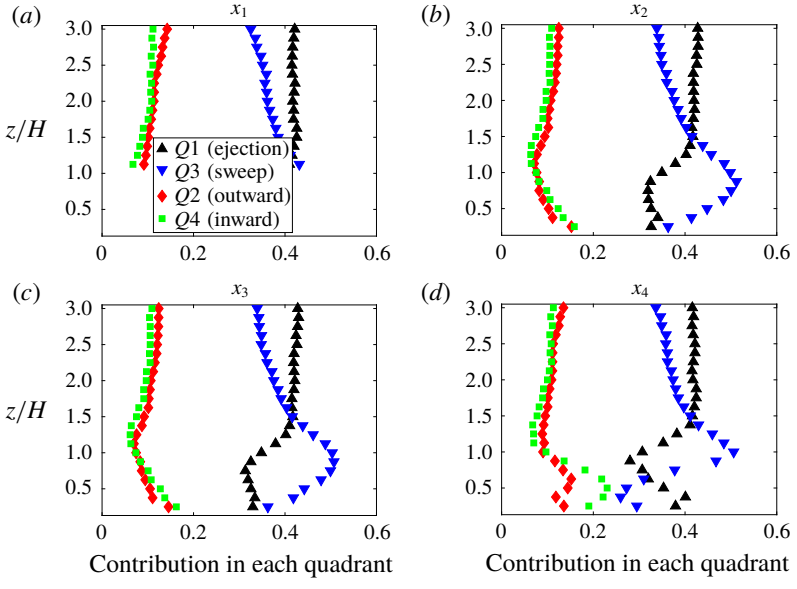

FIGURE 20. (Colour online) Contribution to total flux for scalar for Wide32 (*a–d*) points $x1$–$x4$ indicated in figure 1. Ejections are black △; sweeps are blue ▽; outward interactions are red ◇; and inward interactions are green □.

REFERENCES

ADRIAN, R. J. 2007 Hairpin vortex organization in wall turbulence. *Phys. Fluids* **19** (4), 041301.

ANDERSON, W. 2016 Amplitude modulation of streamwise velocity fluctuations in the roughness sublayer: evidence from large-eddy simulations. *J. Fluid Mech.* **789**, 567–588.

ANDERSON, W., LI, Q. & BOU-ZEID, E. 2015 Numerical simulation of flow over urban-like topographies and evaluation of turbulence temporal attributes. *J. Turbul.* **16** (9), 809–831.

BELCHER, S. E., HARMAN, I. N. & FINNIGAN, J. J. 2012 The wind in the willows: flows in forest canopies in complex terrain. *Annu. Rev. Fluid Mech.* **44**, 479–504.

BOPPANA, V. B. L., XIE, Z. T. & CASTRO, I. P. 2010 Large-eddy simulation of dispersion from surface sources in arrays of obstacles. *Boundary-Layer Meteorol.* **135** (3), 433–454.

BOPPANA, V. B. L., XIE, Z.-T. & CASTRO, I. P. 2012 Large-eddy simulation of heat transfer from a single cube mounted on a very rough wall. *Boundary-Layer Meteorol.* **147** (3), 347–368.

BOSE, S. T. & PARK, G. I. 2018 Wall-modeled large-eddy simulation for complex turbulent flows. *Annu. Rev. Fluid Mech.* **50**, 535–561.

BOU-ZEID, E., HIGGINS, C., HUWALD, H., MENEVEAU, C. & PARLANGE, M. B. 2010 Field study of the dynamics and modelling of subgrid-scale turbulence in a stable atmospheric surface layer over a glacier. *J. Fluid Mech.* **665**, 480–515.

BOU-ZEID, E., MENEVEAU, C. & PARLANGE, M. 2005 A scale-dependent Lagrangian dynamic model for large eddy simulation of complex turbulent flows. *Phys. Fluids* **17** (2), 1–18.

BOU-ZEID, E., VERCAUTEREN, N., PARLANGE, M. B. & MENEVEAU, C. 2008 Scale dependence of subgrid-scale model coefficients: an *a priori* study. *Phys. Fluids* **20** (11), 1–6.

CASTRO, I. P., CHENG, H. & REYNOLDS, R. 2006 Turbulence over urban-type roughness: deductions from wind-tunnel measurements. *Boundary-Layer Meteorol.* **118** (1), 109–131.

CHAMECKI, M. 2013 Persistence of velocity fluctuations in non-Gaussian turbulence within and above plant canopies. *Phys. Fluids* **25** (11).

CHENG, Y., SAYDE, C., LI, Q., BASARA, J., SELKER, J., TANNER, E. & GENTINE, P. 2017 Failure of Taylor's hypothesis in the atmospheric surface layer and its correction for eddy-covariance measurements. *Geophys. Res. Lett.* **44** (9), 4287–4295.

CHESTER, S., MENEVEAU, C. & PARLANGE, M. B. 2007 Modeling turbulent flow over fractal trees with renormalized numerical simulation. *J. Comput. Phys.* **225** (1), 427–448.

CHRISTEN, A., VAN GORSEL, E. & VOGT, R. 2007 Coherent structures in urban roughness sublayer turbulence. *Intl J. Climatol.* **27** (14), 1955–1968.

CHRISTEN, A. & VOGT, R. 2004 Direct measurement of dispersive fluxes within a cork oak plantation. In *26th Conference on Agricultural and Forest Meteorology*, American Meteorological Society.

COCEAL, O., DOBRE, A., THOMAS, T. G. & BELCHER, S. E. 2007*a* Structure of turbulent flow over regular arrays of cubical roughness. *J. Fluid Mech.* **589**, 375–409.

COCEAL, O., THOMAS, T. G. & BELCHER, S. E. 2007*b* Spatial variability of flow statistics within regular building arrays. *Boundary-Layer Meteorol.* **125** (3), 537–552.

DUPONT, S. & PATTON, E. G. 2012 Momentum and scalar transport within a vegetation canopy following atmospheric stability and seasonal canopy changes: the CHATS experiment. *Atmos. Chem. Phys.* **12** (13), 5913–5935.

FANG, J., DIEBOLD, M., HIGGINS, C. & PARLANGE, M. B. 2011 Towards oscillation-free implementation of the immersed boundary method with spectral-like methods. *J. Comput. Phys.* **230** (22), 8179–8191.

FINNIGAN, J. J. 1985 *Turbulent Transport in Flexible Plant Canopies*. pp. 443–480. Springer.

FINNIGAN, J. J. 2003 Turbulence in plant canopies. *Annu. Rev. Fluid Mech.* **32** (1), 519–571.

FINNIGAN, J. J., SHAW, R. H. & PATTON, E. G. 2009 Turbulence structure above a vegetation canopy. *J. Fluid Mech.* **637**, 387.

GHISALBERTI, M. 2009 Obstructed shear flows: similarities across systems and scales. *J. Fluid Mech.* **641**, 51–61.

GIOMETTO, M. G., CHRISTEN, A., MENEVEAU, C., FANG, J., KRAFCZYK, M. & PARLANGE, M. B. 2016 Spatial characteristics of roughness sublayer mean flow and turbulence over a realistic urban surface. *Boundary-Layer Meteorol.* **160** (3), 425–452.

HETSRONI, G., MOSYAK, A., ROZENBLIT, R. & YARIN, L. P. 1999 Thermal patterns on the smooth and rough walls in turbulent flows. *Intl J. Heat Mass Transfer* **42** (20), 3815–3829.

JELLY, T. O. & BUSSE, A. 2018 Reynolds and dispersive shear stress contributions above highly skewed roughness. *J. Fluid Mech.* **852**, 710–724.

JIMÉNEZ, J. 2004 Turbulent flows over rough walls. *Annu. Rev. Fluid Mech.* **36** (1), 173.

KADER, B. A. & YAGLOM, A. M. 1972 Heat and mass transfer laws for fully turbulent wall flows. *Intl J. Heat Mass Transfer* **15** (12), 2329–2351.

KANDA, M. 2006 Large-eddy simulations on the effects of surface geometry of building arrays on turbulent organized structures. *Boundary-Layer Meteorol.* **118** (1), 151–168.

KANDA, M., MORIWAKI, R. & KASAMATSU, F. 2004 Large-eddy simulation of turbulent organized structures within and above explicitly resolved cube arrays. *Boundary-Layer Meteorol.* **112** (2), 343–368.

KANG, H. S. & MENEVEAU, C. 2001 Passive scalar anisotropy in a heated turbulent wake: new observations and implications for large-eddy simulations. *J. Fluid Mech.* **442**, 161–170.

KATUL, G. G., HSIEH, C. I. & KUHN, G. 1997*a* Turbulent eddy motion at the forestatmosphere interface. *J. Geophys*.

KATUL, G. G., KUHN, G., SCHIELDGE, J. & HSIEH, C. I. 1997*b* The ejection-sweep character of scalar fluxes in the unstable surface layer. *Boundary-Layer Meteorol*.

LEONARDI, S. & CASTRO, I. P. 2010 Channel flow over large cube roughness: a direct numerical simulation study. *J. Fluid Mech.* **651**, 519–539.

LEONARDI, S., ORLANDI, P., DJENIDI, L. & ANTONIA, R. A. 2015 Heat transfer in a turbulent channel flow with square bars or circular rods on one wall. *J. Fluid Mech.* **776**, 512–530.

LI, D. 2016 Revisiting the subgrid-scale Prandtl number for large-eddy simulation. *J. Fluid Mech.* **802**, R2.

LI, D. & BOU-ZEID, E. 2011 Coherent structures and the dissimilarity of turbulent transport of momentum and scalars in the unstable atmospheric surface layer. *Boundary-Layer Meteorol.* **140** (2), 243–262.

LI, Q., BOU-ZEID, E. & ANDERSON, W. 2016*a* The impact and treatment of the Gibbs phenomenon in immersed boundary method simulations of momentum and scalar transport. *J. Comput. Phys.* **310**, 237–251.

LI, Q., BOU-ZEID, E., ANDERSON, W., GRIMMOND, S. B. & HULTMARK, M. 2016*b* Quality and reliability of les of convective scalar transfer at high Reynolds numbers. *Intl J. Heat Mass Transfer* **102**, 959–970.

LLAGUNO-MUNITXA, M. & BOU-ZEID, E. 2018 Shaping buildings to promote street ventilation: a large-eddy simulation study. *Urban Clim.* **26**, 76–94.

LLAGUNO-MUNITXA, M., BOU-ZEID, E. & HULTMARK, M. 2017 The influence of building geometry on street canyon air flow: validation of large eddy simulations against wind tunnel experiments. *J. Wind Engng Ind. Aerodyn.* **165**, 115–130.

MACDONALD, R. W. & GRIFFITHS, R. F. 1998 An improved method for the estimation of surface roughness of obstacle arrays. *Atmos. Environ* **32** (11), 1838–2042.

MARTILLI, A. & SANTIAGO, J. L. 2007 CFD simulation of airflow over a regular array of cubes. Part II: analysis of spatial average properties. *Boundary-Layer Meteorol.* **122** (3), 635.

MITTAL, R., DONG, H., BOZKURTTAS, M., NAJJAR, F. M., VARGAS, A. & VON LOEBBECKE, A. 2008 A versatile sharp interface immersed boundary method for incompressible flows with complex boundaries. *J. Comput. Phys.* **227** (10), 4825–4852.

MITTAL, R. & IACCARINO, G. 2005 Immersed boundary methods. *Annu. Rev. Fluid Mech.*

MOHD-YUSOF, J. 1997 Combined immersed-boundary/B-spline methods for simulations of flow in complex geometries. In *Center for Turbulence Research Annual Research Briefs*, pp. 317–327, NASA Ames/Stanford University.

MOURI, H., TAKAOKA, M., HORI, A. & KAWASHIMA, Y. 2003 Probability density function of turbulent velocity fluctuations in a rough-wall boundary layer. *Phys. Rev.* E **68** (3), 6.

NAGANO, Y. & TAGAWA, M. 1988 Statistical characteristics of wall turbulence with a passive scalar. *J. Fluid Mech.* **196**, 157–185.

ORLANDI, P. & LEONARDI, S. 2008 Direct numerical simulation of three-dimensional turbulent rough channels: parameterization and flow physics. *J. Fluid Mech.* **606**, 399–415.

PARK, S. B. & BAIK, J. J. 2013 A large-eddy simulation study of thermal effects on turbulence coherent structures in and above a building array. *J. Appl. Meteorol. Climatol.* **52** (6), 1348–1365.

PERRET, L., BASLEY, J., MATHIS, R. & PIQUET, T. 2019 The atmospheric boundary layer over urban-like terrain: influence of the plan density on roughness sublayer dynamics. *Boundary-Layer Meteorol.* **170** (2), 205–234.

PERRY, A. E. & HOFFMANN, P. H. 1976 An experimental study of turbulent convective heat transfer from a flat plate. *J. Fluid Mech.* **77** (2), 355–368.

PHILIPS, D. A., ROSSI, R. & IACCARINO, G. 2013 Large-eddy simulation of passive scalar dispersion in an urban-like canopy. *J. Fluid Mech.* **723**, 404–428.

PIROZZOLI, S., BERNARDINI, M. & ORLANDI, P. 2016 Passive scalars in turbulent channel flow at high Reynolds number. *J. Fluid Mech.* **788**, 614–639.

PLACIDI, M. & GANAPATHISUBRAMANI, B. 2015 Effects of frontal and plan solidities on aerodynamic parameters and the roughness sublayer in turbulent boundary layers. *J. Fluid Mech.* **782**, 541–566.

POGGI, D. & KATUL, G. G. 2008 The effect of canopy roughness density on the constitutive components of the dispersive stresses. *Exp. Fluids* **45** (1), 111–121.

POGGI, D., KATUL, G. G. & ALBERTSON, J. D. 2004 A note on the contribution of dispersive fluxes to momentum transfer within canopies. *Boundary-Layer Meteorol.* **111** (3), 615–621.

POKRAJAC, D., CAMPBELL, L. J., NIKORA, V., MANES, C. & MCEWAN, I. 2007 Quadrant analysis of persistent spatial velocity perturbations over square-bar roughness. *Exp. Fluids* **42** (3), 413–423.

RAUPACH, M. R. 1981 Conditional statistics of Reynolds stress in rough-wall and smooth-wall turbulent boundary layers. *J. Fluid Mech.* **108**, 363–382.

RAUPACH, M. R., FINNIGAN, J. J. & BRUNEI, Y. 1996 Coherent eddies and turbulence in vegetation canopies: the mixing-layer analogy. *Boundary-Layer Meteorol.* **78** (3–4), 351–382.

ROTACH, M. W. 1993 Turbulence close to a rough urban surface part I: Reynolds stress. *Boundary-Layer Meteorol.* **65** (1–2), 1–28.

TSENG, Y. H., MENEVEAU, C. & PARLANGE, M. B. 2006 Modeling flow around bluff bodies and predicting urban dispersion using large eddy simulation. *Environ. Sci. Technol.* **40** (8), 2653–2662.

WALLACE, J. M. 2016 Quadrant analysis in turbulence research: history and evolution. *Annu. Rev. Fluid Mech.* **48** (1), 131.

WANG, L., LI, D., GAO, Z., SUN, T., GUO, X. & BOU-ZEID, E. 2014 Turbulent transport of momentum and scalars above an urban canopy. *Boundary-Layer Meteorol.* **150** (3), 485–511.

WANG, W., SMITH, J. A., RAMAMURTHY, P., BAECK, M. L., BOU-ZEID, E. & SCANLON, T. M. 2016 On the correlation of water vapor and c02: application to flux partitioning of evapotranspiration. *Water Resour. Res.* **52** (12), 9452–9469.

WILSON, N. R. & SHAW, R. H. 1977 A higher order closure model for canopy flow. *J. Appl. Meteorol.* **16** (11), 1197–1205.

WYNGAARD, J. C. & MOENG, C.-H. 1992 Parameterizing turbulent diffusion through the joint probability density. *Boundary-Layer Meteorol.* **60** (1-2), 1–13.

YANG, X., SADIQUE, J., MITTAL, R. & MENEVEAU, C. 2015 Integral wall model for large eddy simulations of wall-bounded turbulent flows. *Phys. Fluids* **27** (2), 025112.

YANG, X., SADIQUE, J., MITTAL, R. & MENEVEAU, C. 2016 Exponential roughness layer and analytical model for turbulent bounday layer flow over rectangular-prism roughness elements. *J. Fluid Mech.* **789**, 127–165.

YUAN, J. & JOUYBARI, M. A. 2018 Topographical effects of roughness on turbulence statistics in roughness sublayer. *Phys. Rev. Fluids* **3** (11), 114603.

ZHU, X., IUNGO, G. V., LEONARDI, S. & ANDERSON, W. 2017 Parametric study of urban-like topographic statistical moments relevant to *a priori* modelling of bulk aerodynamic parameters. *Boundary-Layer Meteorol.* **162** (2), 231–253